Guest–host interactions of a rigid organic molecule in porous silica frameworks

Di Wu[a,b], Son-Jong Hwang[c], Stacey I. Zones[d,e], and Alexandra Navrotsky[a,b,1]

[a]Peter A. Rock Thermochemistry Laboratory and Nanomaterials in the Environment, Agriculture, and Technology Organized Research Unit (NEAT ORU), University of California, Davis, CA 95616; [b]Department of Chemical Engineering and Materials Science, University of California, Davis, CA 95616; [c]Division of Chemistry and Chemical Engineering, California Institute of Technology, Pasadena, CA 91125; [d]Catalyst Department, Chevron Energy Technology Company, Richmond, CA 94802; and [e]Department of Chemical and Biomolecular Engineering, University of California, Berkeley, CA 94720

Contributed by Alexandra Navrotsky, December 23, 2013 (sent for review October 23, 2013)

Molecular-level interactions at organic–inorganic interfaces play crucial roles in many fields including catalysis, drug delivery, and geological mineral precipitation in the presence of organic matter. To seek insights into organic–inorganic interactions in porous framework materials, we investigated the phase evolution and energetics of confinement of a rigid organic guest, N,N,*N*-trimethyl-1-adamantammonium iodide (TMAAI), in inorganic porous silica frameworks (SSZ-24, MCM-41, and SBA-15) as a function of pore size (0.8 nm to 20.0 nm). We used hydrofluoric acid solution calorimetry to obtain the enthalpies of interaction between silica framework materials and TMAAI, and the values range from −56 to −177 kJ per mole of TMAAI. The phase evolution as a function of pore size was investigated by X-ray diffraction, IR, thermogravimetric differential scanning calorimetry, and solid-state NMR. The results suggest the existence of three types of inclusion depending on the pore size of the framework: single-molecule confinement in a small pore, multiple-molecule confinement/adsorption of an amorphous and possibly mobile assemblage of molecules near the pore walls, and nanocrystal confinement in the pore interior. These changes in structure probably represent equilibrium and minimize the free energy of the system for each pore size, as indicated by trends in the enthalpy of interaction and differential scanning calorimetry profiles, as well as the reversible changes in structure and mobility seen by variable temperature NMR.

mesoporous silica | thermodynamics | porous materials

Knowing both the structure and molecular mobility of guest matter in nanosized pores and channels, which often differ from those in the bulk unconfined material or solution, is essential for fundamental understanding of processes in both science and technology, with applications including natural processes such as biomineralization (1–3) and membrane transport (4, 5), engineering processes such as oil recovery (6–8), CO_2 sequestration (9–11), catalysis (12–14), and biomedical processes including diagnostics and drug delivery (15–17). Most of the pioneering research has used soft matter as guests, including gas and liquid phases, low-melting point organic solids, and long-chain polymers (18–20).

In our earlier studies, various calorimetric methods have been designed to investigate guest–host interactions. Piccione et al. (21) developed a novel system for hydrofluoric acid (HF) solution calorimetry to study the interactions of four different silica zeolite frameworks with several quaternary ammonium structure-directing agents (SDAs). The enthalpies of interaction were measured to be −32.0 to −181.0 kJ per mole of SDA. Slightly stronger interactions were found by Trofymluk et al. (22) for mesoporous silica phases containing long-chain molecules. Recently, Wu et al. (23) measured the enthalpy of interaction of various small molecules with mesoprous silicas using immersion calorimetry. The hydration enthalpies of a series of cation exchanged aluminosilicate or gallosilicate zeolites were studied by Sun et al. and Zhou et al. (24–27). The data suggest that water is confined energetically more tightly when Al or Ga and a charge-balancing extraframework alkali cation are present compared with pure silica.

Here we take a somewhat different approach. We use a rigid, ionic, organic solid compound, N,N,*N*-trimethyl-1-adamantammonium iodide (TMAAI), with high melting point as guest. The $TMAA^+$ cation is almost spherical and of a diameter comparable to pores in zeolites, and TMAAI is analogous to several SDAs used in zeolite synthesis (28). Our goal is to track the changes in energetics, structure, and mobility as this molecule is introduced into hosts of increasing pore size. The samples were characterized by powder X-ray diffraction (XRD), infrared spectroscopy (FTIR), and thermal analysis [thermogravimetric differential scanning calorimetry (TG-DSC)]. HF solution calorimetry has been used to investigate quantitatively the energetics of guest–host interactions of TMAAI in a series of porous silicas (SSZ-24, MCM-41, and SBA-15), with pores from 0.8 to 20.0 nm in diameter. Solid-state NMR experiments monitored changes in molecular motion upon confinement at temperature from −90 to 140 °C.

Results

The calculated properties of all calcined mesoporous silica samples from nitrogen adsorption/desorption data based on the Brunauer–Emmett–Teller theory (29) and Barrett–Joyner–Halenda method (30, 31) are listed in Table 1. The results confirm that all analyzed calcined mesoporous silica samples have uniform pore structure with narrow pore size distribution.

The powder XRD patterns of calcined mesoporous silicas confirm that all samples are 2D hexagonal (*p6mm*) ordered structures (Fig. S1). They also indicate that after calcination, all porous silica samples maintain their structure without degradation.

Significance

Confinement of molecules in nanoscale pores is important in both science and technology. This paper reports a systematic analysis of the structural, thermodynamic, and dynamic behavior on confinement of a rigid organic molecule in a series of silica frameworks with different pore sizes (0.8 to 20.0 nm). The comprehensive data set enables the strength of guest–host interactions to be calculated; structure, phase, and dynamics of confined guests in pores of various diameters to be analyzed; and different types of inclusion to be described. The evolution from single-molecule confinement to multimolecule adsorption/confinement to nanocrystal confinement is documented. This provides a conceptual model linking confinement on various length scales.

Author contributions: D.W., S.I.Z., and A.N. designed research; D.W. and S.-J.H. performed research; D.W., S.-J.H., S.I.Z., and A.N. contributed new reagents/analytic tools; D.W., S.-J.H., S.I.Z., and A.N. analyzed data; and D.W. and A.N. wrote the paper.

The authors declare no conflict of interest.

[1]To whom correspondence should be addressed. E-mail: anavrotsky@ucdavis.edu.

This article contains supporting information online at www.pnas.org/lookup/suppl/doi:10.1073/pnas.1323989111/-/DCSupplemental.

Table 1. Properties of calcined porous silica framework hosts studied and calculated enthalpies of interaction for porous silica framework hosts with TMAAI guest at 50 °C

Framework host	Pore size, nm	Pore volume, cm^3/g	Surface area, m^2/g	$\Delta H_{int\ TMAAI/SiO2}$, kJ/mol TMAAI	$\Delta H_{int\ TMAAI/SiO2}$, kJ/mol SiO_2
SSZ-24	0.8	0.1	316.8	−176.54 ± 15.08	−4.89 ± 0.42
MCM-41	2.2	0.7	1,544.6	−76.01 ± 10.30	−3.21 ± 0.44
SBA-15_1	6.6	1.2	672.4	−55.61 ± 8.57	−3.91 ± 0.60
SBA-15_2	12.8	1.8	486.3	−122.70 ± 10.51	−12.62 ± 1.08
SBA-15_3	20.0	2.3	530.7	−148.01 ± 10.19	−19.16 ± 1.05

Enthalpies of interaction are per mole of guest molecules or SiO_2.

The combination of TGA, DSC, XRD, and FTIR allows us to quantify the organic content and identify the phase of nanoconfined TMAAI. The organic contents of as-made SSZ-24 and TMAAI-containing mesoporous silica samples obtained from TGA (Fig. 1*A*) and the calculated volume fraction of pores and molar formulas are listed in Table S1. The weight losses below 150 °C represent dehydration of loosely bound water and are less than 0.85 wt % for all samples.

DSC traces (140–280 °C in argon; Fig. 1*B*) all show similar thermal behavior with endothermic peaks between 240 and 280 °C. These thermal events reflect phase transitions and molecular motion changes of confined TMAAI molecules. The observed melting points of nanoconfined TMAAI in mesoporous silicas are lower than for bulk TMAAI (311 °C), with the melting temperature depression generally increasing with decreasing pore size (Fig. 1*C*). The DSC peaks tend to be broader for TMAAI confined in frameworks with smaller pores. Due to quick evaporation of TMAAI after melting, quantification of enthalpy of fusion proved to be not possible.

DSC traces at low temperature (−80–40 °C) are shown in Fig. 1*D*. Although peaks are not very well resolved, broad endothermic heat events are visible between −80 and 40 °C for TMAAI-containing MCM-41 and SBA-15_1. These may be an indication of continuously decreasing mobility with decreasing temperature and possible transition to solid-like phases for the small amounts of TMAAI confined in these two frameworks with smaller primary pore sizes.

The powder XRD patterns of TMAAI-containing mesoporous silica samples are shown in Fig. 1*E*. For TMAAI-containing MCM-41 (2.2 nm) and SBA-15_1 (6.6 nm), no significant additional peaks (other than those corresponding to the periodicity of cylindrical pores) are observed. However, the XRD patterns of TMAAI-containing SBA-15_2 (12.8 nm) and SBA-15_3 (20.0 nm) confirm the presence of nanocrystalline TMAAI by relatively broad and shifted diffraction peaks compared with patterns of the bulk phase. The crystallite sizes were calculated using the Scherrer formula (32) to be 11.6 nm for SBA-15_2 (12.8-nm pore) and 18.3 nm for SBA-15_3 (20.0-nm pore). Within estimated experimental error, the crystallite size and pore size are the same; thus, a single nanocrystal fills the pore.

Infrared absorbance spectra (Fig. 1*F*) were obtained by subtracting spectra of their calcined forms as background. The bands at 2,917 and 2,856 cm^{-1} are attributed to CH and CH_2 stretching vibrations from the adamantane core. Only the two TMAAI-containing mesoporous silica samples with crystalline XRD peaks show a band at 3,018 cm^{-1} which is assigned to the *N*-CH_3 moiety in the spectrum of TMAAI bulk crystal. For the two frameworks with smaller pore sizes, this band is obscured or broadened by the hydrogen bonding between the nitrogen atom and the silanol groups on silica surfaces. This observation further supports the presence of a nanocrystalline phase in the mesoporous silica frameworks with larger primary pores.

Fig. 2 shows room temperature ^1H and ^{13}C magic angle spinning (MAS) NMR spectra of bulk TMAAI and TMAAI-containing silica samples. The stacked plots reveal progressive changes in spectral resolution as the organic molecule is located in various environments from bulk to single molecule confined in a zeolite pore. The ^1H MAS NMR spectra show the sharpest peaks for SSZ-24 and the broadest for the bulk crystalline solid, whereas progressive broadening is observed for mesoporous samples with increasing pore size, indicating increasing intermolecular ^1H–^1H dipolar coupling. The ^{13}C MAS NMR spectra contain one primary isotropic peak at ∼50 ppm, as a result of the selective ^{13}C labeling at the *N*-methyl carbon for all samples except SSZ-24. The shape of this peak, sharp or broad, represents the shielding environment of the carbon atom and indicates order–disorder around a TMAAI molecule. For bulk TMAAI, a sharp signal [full width at half maximum (FWHM) = 22 Hz] typical for a crystalline solid is observed. For SSZ-24, the ^{13}C signal shows noticeable increase in line width (146 Hz) and upfield shift by ∼2 ppm. The same carbon signal becomes even broader for MCM-41 (238 Hz) and SBA-15_1 (268 Hz). The broad nature of the ^{13}C signal is believed to originate from the distribution of isotropic resonances and subsequently reflects the disordered or amorphous nature of the structure around TMAAI when confined in pores smaller than 12.0 nm. TMAAI in SBA-15_2 and 3 shows coexistence of both sharp and broad ^{13}C signals, suggesting the presence of both crystalline and amorphous phases when confined in bigger pores. The peak intensities directly represent the ratio of the amounts

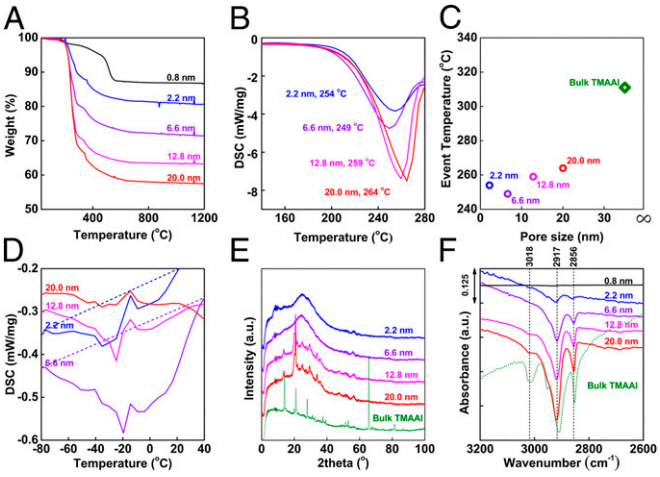

Fig. 1. (*A*) TGA curves (30–1,200 °C, in air at 10 °C/min) of TMAAI-containing porous silica samples. (*B*) DSC traces (140–280 °C, in argon at 10 °C/min) of TMAAI-containing mesoporous silica samples. (*C*) Melting points of nanoconfined TMAAI in mesoporous silica framework hosts vs. framework pore size. Melting point of TMAAI bulk crystal (311 °C) is represented as ◇. (*D*) DSC traces (−80–40 °C, under helium at 10 °C/min) of TMAAI-containing mesoporous silica samples. Broad areas under the dashed lines represent magnitude of potential endothermic heat events. (*E*) Powder XRD patterns (0.5–100°) of TMAAI-containing mesoporous silica samples and TMAAI bulk crystal at room temperature. (*F*) IR absorbance spectra of TMAAI-containing porous silica samples and TMAAI bulk crystal at room temperature.

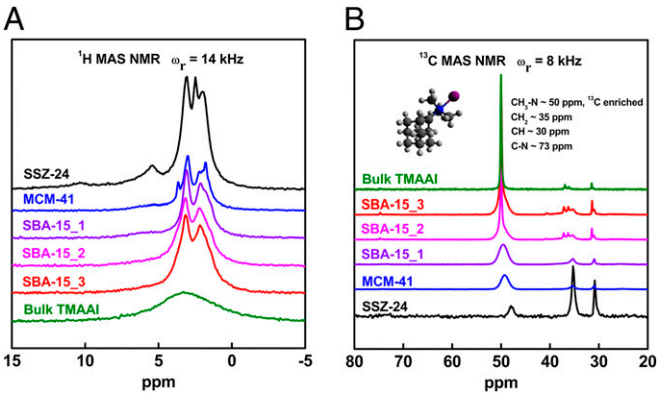

Fig. 2. (*A*) ^{1}H and (*B*) ^{13}C MAS NMR spectra of TMAAI in various confinement environments at 25 °C. The ^{13}C enriched TMAAI on trimethyl groups are used except for SSZ-24.

of amorphous to crystalline phase: 1:1 for SBA-15_2 and 1:1.2 for SBA-15_3 (Fig. 2*B*). Thermal treatment at 140 °C under vacuum indicates no redistribution of phases (Fig. S2). This suggests that either the redistribution has very slow kinetics or the observed distribution represents equilibrium.

The mobility (dynamics) of confined TMAAI molecules was further studied by variable temperature (VT) MAS NMR and spin–lattice relaxation time (T_1) measurements. The ^{1}H and ^{13}C MAS NMR spectra collected at 7.0 T from −90 to 140 °C are compiled in Figs. S3–S5, respectively. Fig. 3 shows the temperature dependence of spectral line width (FWHM) and chemical shift obtained from spectral decomposition of ^{13}C VT MAS NMR spectra. The spectrum of bulk TMAAI shows no variation in ^{1}H VT MAS NMR, whereas the signal of the *N*-methyl carbon at about 50 ppm in the ^{13}C VT MAS NMR shows gradual broadening and downfield shift in peak position with increasing temperature. The broadening stops above room temperature. For TMAAI confined in isolated pores of SSZ-24 (0.8 nm), as temperature increases, there is hardly any variation in width of both ^{1}H and ^{13}C signals, suggesting minimum mobility change of TMAAI in a tightly constrained environment. In sharp contrast, when TMAAI is confined as an amorphous phase in mesopores less than 12.0 nm (MCM-41 and SBA-15_1), noticeable changes in peak widths are visible as temperature varies. For these medium pore samples, both ^{1}H and ^{13}C MAS NMR show a sudden narrowing at around 70 °C, indicating a relatively sharp increase in mobility. The ^{1}H and ^{13}C MAS NMR spectra of confined TMAAI in pores larger than 12.0 nm (SBA-15_2 and SBA-15_3) are more complicated. Because there is no redistribution of phases in the temperature range investigated, spectral fitting is applicable (Fig. 3 and Fig. S5). Confined nanocrystals in SBA-15_3 and bulk TMAAI show nearly identical temperature dependence for both FWHM and chemical shift. Although they show no motional narrowing at temperatures greater than −20 °C, below −20 °C, noticeable freezing behavior was observed. These observations not only support our peak assignments but also imply that NMR cannot discriminate nanocrystals from bulk crystals because this spectroscopy probes mainly short range order. On the other side, the broad ^{13}C peak corresponding to the amorphous phase in nanocrystal-containing samples is similar to that of the amorphous TMAAI confined in MCM-41 and SBA-15_1. The significant reduction of FWHM (Fig. 3*A*) at about 70 °C is more clearly seen for the amorphous TMAAI in SBA-15_3. However, chemical shift changes (Fig. 3*B*) with temperature do not differentiate the amorphous phase from the crystalline phase, especially for the slope (ppm/T). All samples show chemical shifts indicative of better chemical shielding as temperature decreases and the shielding of *N*-methyl carbon appears to grow (upfield shift) as the pore size decreases for molecules in the amorphous phase.

The ^{1}H and ^{13}C T_1 relaxation times were measured for all samples (Fig. 3 *C* and *D*). T_1 varies as a function of temperature as a result of changes in atomic or molecular motion and reaches a minimum when the motional correlation time becomes equal to the NMR frequency. Because all peaks between 0 and 5 ppm show nearly the same behavior, ^{1}H T_1 relaxation times reported here represent the median value that is associated with motion of the whole molecule rather than that of a particular segment. The ^{13}C T_1 relaxation times were measured only for ^{13}C labeled *N*-methyl carbons. As shown in Fig. 3, bulk TMAAI presents ^{1}H and ^{13}C T_1 curves typical of organic solids over the temperature range applied. Upon confinement, TMAAI exhibits much wider ^{1}H T_1 curves, which suggest smaller activation energy for the specific molecular motion. Although there are only very slight differences in the ^{1}H T_1 curves for confined TMAAI above room temperature, there is noticeable distinction at lower temperature. The difference in activation energies obtained from ^{1}H T_1 fits of the bulk TMAAI and its nanocrystalline phase in SBA-15_3 is about 10 kJ/mol. The ^{13}C T_1 data (Fig. 3*D*) show a similar temperature dependence for both bulk and confined nanocrystalline phases, whereas the temperature for optimum relaxation is shifted by about 40 °C, resulting in a slight difference in the activation energy (~3 kJ/mol) of the motion of *N*-methyl carbons. Additionally, the T_1 behavior of the amorphous phase in SBA-15_3 is similar to that of TMAAI confined in pores smaller than 12.0 nm.

Table S2 summarizes calorimetric data for both calcined and TMAAI-containing samples. The measured enthalpies of solution (per mole of SiO_2) for calcined porous silica samples range from −147.5 ± 0.3 to −166.4 ± 0.9 kJ/mol and for TMAAI-containing porous silicas from −142.6 ± 0.3 to −158.6 ± 0.2 kJ/mol. The enthalpies of interaction between porous silica hosts and TMAAI guest were calculated using the thermodynamic cycle described in *SI Materials and Methods*. The enthalpies of solution

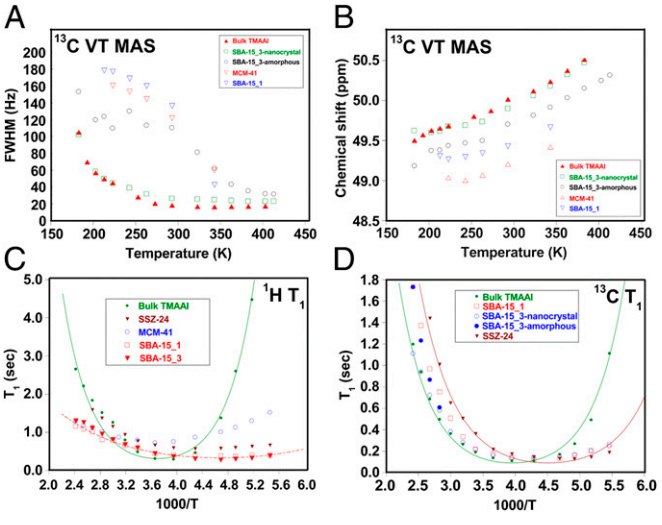

Fig. 3. Temperature dependence of (*A*) ^{13}C MAS NMR spectral line width (FWHM) and (*B*) chemical shifts for bulk crystalline TMAAI, amorphous phase in MCM-41 and SBA-15_1, and nanocrystalline and amorphous phases found in SBA-15_3. Spin–lattice relaxation time (T_1) of (*C*) ^{1}H and (*D*) ^{13}C spins of *N*-trimethyl groups of TMAAI in various confined environments. The corresponding values of fit parameters were $\tau_o = 4 \times 10^{-14}$ s, $E_a = 19.5$ kJ/mol (±1.3), for ^{1}H relaxation curve of the bulk TMAAI, and $\tau_o = 4.6 \times 10^{-12}$ s, $E_a = 7.4$ kJ/mol (±0.6), for SBA-15_3. Similarly, parameters from ^{13}C T_1 fitting were 8.1×10^{-14} s, 17.3 kJ/mol, and 6.9×10^{-14} s, 15.4 kJ/mol, for the bulk TMAAI and SSZ-24, respectively.

of calcined porous silicas are all exothermic; calcined silica samples with larger primary pores tend to have more exothermic enthalpies of solution than those with smaller pores. Thus, calcined porous silica samples with larger primary pores are energetically less stable than those with smaller pore sizes, in accord with earlier observations (22). The solution enthalpies of TMAAI-containing porous silica samples are less exothermic than those of their respective empty calcined porous silica frameworks, with TMAAI-containing SBA-15_1 giving the most exothermic value (-158.6 ± 0.2 kJ per mole of SiO_2) and TMAAI-containing SSZ-24 being least exothermic (-142.6 ± 0.3 kJ per mole of SiO_2).

Table 1 summarizes the enthalpies of interaction of calcined porous silicas with TMAAI calculated using TMAAI contents derived from thermogravimetric analyses. The enthalpies of interaction (per mole of TMAAI) versus primary framework pore size are plotted in Fig. 4*A*. Porous silica with pore size from 0.8 to 20.0 nm has enthalpies of interaction from -55.6 ± 8.6 to -176.5 ± 15.1 kJ per mole of TMAAI and -3.2 ± 0.4 to -19.2 ± 1.1 kJ per mole of SiO_2. In SBA-15, the enthalpies of interaction per mole of TMAAI or SiO_2 tend to be more exothermic as the primary pore size increases.

Discussion

The detailed set of experimental observations allows us to develop a consistent model for the structure, energetics, and dynamics of TMAAI in porous silica. For mesoporous silica having pores smaller than 12.0 nm, TMAAI appears to be amorphous; in other words, the guest preserves high entropy but receives some geometric constraint and moderate energetic stabilization from the host framework. Such a layer of disordered molecules is probably near the pore walls. On the other hand, noting the coexistence of crystalline and disordered TMAAI domains in pores larger than 12.0 nm and considering all of the experimental results, we conclude that the confined TMAAI molecules form nanocrystalline cores, presumed to be at or near the center of the pores, whereas the amorphous TMAAI fills the space between the silica pore wall and the "crystalline core." The reproducibility and reversibility of the temperature-dependent spectral features argues that equilibrium is maintained and the system seeks the configuration of lowest free energy for a given pore size, with the crystalline/amorphous nature of the guest molecules playing a contributing role.

Porous materials are stabilized by adsorbed species; in return, the pore structure also modifies the physical properties and structure of confined guests. Earlier studies by DSC pointed out that melting point depression of bulk materials in a nanoconfined environment is common for both liquid and solid guest phases, including water (33–35), benzene (36, 37), cyclohexane (36), heptanes (36), *o*-terphenyl (38), benzyl alcohol (38), ibuprofen (36, 39), and glycine (40). Similar behavior was also found in a system containing metal clusters; confined iridium clusters in controlled-pore glass showed lower melting point as pore size decreased (41). Elevation of melting point is also possible in nanoscale confinement. For example, Alba-Simionesco et al. reported that when confined in activated carbon fibers, the melting point of benzene was elevated (37). Polymorphism of confined guest molecules in porous materials has been observed for decades. Most early studies used liquid phase guests, and the experiments were performed at temperature below 0 °C (37, 38, 42). Recently, organic guest compounds with several polymorphs under nanoconfinement were also studied in different systems, in which pore size effect and kinetic factors were discussed (43–45). These reports noted that pore size, guest–host interactions, and surface properties of the pore wall are crucial factors to determine the final guest phases. However, few quantitative data were provided. The present study provides such needed quantitation.

Observations from XRD and DSC reveal the phase evolution of TMAAI as a function of pore size. XRD patterns strongly suggest that TMAAI in silicas with smaller pore sizes (2.2 and 6.6 nm) are amorphous, whereas frameworks with larger pores (12.8 and 20.0 nm) contain confined nanocrystalline TMAAI somewhat different in lattice spacing from bulk material. The possibility that there is crystalline TMAAI material outside the silica frameworks is ruled out by the absence of any Bragg reflections corresponding in position to that of bulk TMAAI. In addition, the DSC curves of samples with amorphous TMAAI show significant melting point broadening which is a characteristic feature of amorphous phases. Strictly speaking, the term "melting point" involved here is merely a notation of average temperature of a series of motion and phase transition, which is represented by the center of DSC peaks. The highest melting point depression (61 °C) is seen in MCM-41. This observation further supports that confined TMAAI is amorphous in MCM-41 and SBA-15_1. On the other hand, DSC results indicate that TMAAI crystallizes within the larger pores.

According to the Gibbs–Thomson equation,

$$\Delta T_m = T_{m(\text{bulk})} - T_{m(r_{\text{pore}})} = \frac{2V_m T_{m(\text{bulk})}(\gamma_{\text{lw}} - \gamma_{\text{cw}})}{r_{\text{pore}} \Delta H_m}.$$

$T_{m(\text{bulk})}$ represents the melting point of bulk phase, $T_{m(r_{\text{pore}})}$ is the melting point of the same material confined in nanopores with a radius r, ΔH_m is the molar melting enthalpy of the bulk phase, and V_m is the molar volume of the bulk crystal. γ_{lw} and γ_{cw} are the liquid–wall and crystal–wall interaction energies, respectively. If $\gamma_{\text{cw}} > \gamma_{\text{lw}}$, the melting point of this nanocrystalline phase is depressed, and the confined nanocrystalline material should nucleate at the center of the pore. When $\gamma_{\text{cw}} < \gamma_{\text{lw}}$, the crystallized nanosized solid would be coated onto the pore wall, forming a very stable phase with elevated melting point. The observed decrease of TMAAI melting temperature with decreasing pore size suggests that the wetting angle between the TMAAI crystals and the TMAAI-coated silica layer is between 90 and 180°, and the crystallized TMAAI stays near the center of the pore. Furthermore, calorimetric evidence (Fig. 4*A*) also suggests a significant change of the enthalpy of interaction when the pore size is larger than 12.0 nm. Therefore, we have enough evidence to conclude that TMAAI in pores smaller than 12.0 nm is amorphous, whereas it partially crystallizes in larger pores, forming crystals in the center of the channels with some amorphous material near the walls.

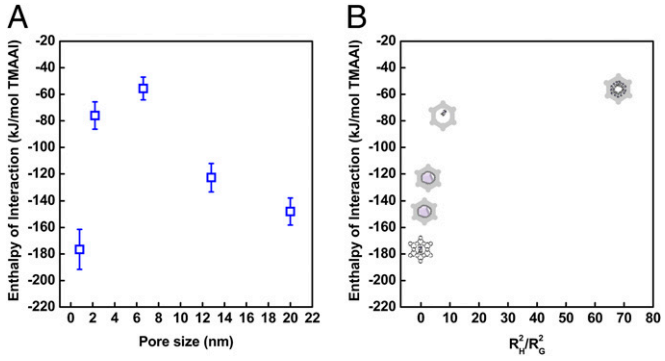

Fig. 4. (*A*) Enthalpies of interaction for porous silica samples per mole of TMAAI vs. pore size. (*B*) Enthalpies of interaction for porous silica samples per mole of TMAAI vs. (pore size/guest size)^2 with schematic representation of structures of guest–host interaction in the pores of each sample. For SSZ-24, MCM-41, and SBA-15_1, molecular TMAAI is confined; in SBA-15_2 and 3, TMAAI forms nanocrystals reaching the size limitation imposed by the pore diameter. Dimensions in schematics are approximate.

Previous studies indicated that similar phase separation and structures of confined compounds were also found in various silica matrices. As early as the 1960s, Litvan et al. reported that confined water molecules bond strongly onto the wall of silica pores and show nonbulk behavior (46). In later reports, Rennie et al. suggested that in addition to the tightly bound water near the pore walls, the water at the center of the pores showed behavior similar to that of bulk water, with greater mobility (33). Additionally, recent work by Erko et al. revealed that upon confinement, water showed a two-step density profile with two layers of water near the pore wall having higher density than the core water (47). Azaïs et al. demonstrated that once confined in MCM-41 (11.6 nm), ibuprofen was not totally crystalline; instead, a small fraction of glassy ibuprofen was present (42). Thus, the coexistence of two phases under nanoconfinement, with the more ordered material near the center of the pore and the less ordered material near the wall, may be a general feature, although the details will depend on the specific system under study. Solid-state NMR data further support the above conclusions from structural and thermal analyses by providing local order information at the molecular level.

The enthalpies of interaction between TMAAI and silicas correlate roughly linearly with pore size for pores smaller than 12.0 nm (Fig. 4*A*). In this region, the amorphous TMAAI interacts more strongly with the framework as pore size decreases. However, for samples SBA-15_2 and 3 the trend is reversed and these samples contain nanocrystalline TMAAI. All of the observations from XRD, DSC, IR, NMR, and HF calorimetry strongly suggest that the strongest confinement effects are not always in hosts with smaller pores; the phase (amorphous or crystalline) of confined guests is also crucial. Indeed, supposing the enthalpy of interaction follows the trend defined by MCM-41 and SBA-15_1, for pores larger than 12.0 nm the enthalpies of interaction will approach or exceed zero. Such weak interactions won't be able to effectively stabilize the confined TMAAI molecules.

To further analyze steric effects, a dimensionless term V_H/V_G is introduced, which represents the relative size of host pores and guest objects. V_H and V_G are defined as "effective volume," which means the actual volume involved in the guest–host interactions. In our specific system, the shapes of both of the molecules/crystals and pores/channels can be treated as spherical or cylindrical. Assuming there is negligible interaction in the axial direction, the term V_H/V_G can be reduced to $(R_H/R_G)^2$, in which R_G and R_H represent the radii of guest molecules and host pores, respectively.

In Fig. 4*B*, the enthalpies of interaction between TMAAI and silica frameworks are plotted versus $(R_H/R_G)^2$. The data exhibit a roughly exponential trend. For this plot, two extreme conditions need to be mentioned. When $(R_H/R_G)^2 = 1$, the guest and host contact each other tightly, for example, embedded TMAAI in SSZ-24 or confined nanocrystals in SBA-15_2 and 3. The host channels then apply great confinement effects on the guest objects. When $(R_H/R_G)^2$ approaches infinity, the host dimension is much greater than the guest, and the confinement effect is minimized. This would be the case when a molecule or cluster or nanocrystal is adsorbed on a uniform flat surface. If $(R_H/R_G)^2$ is between 1 and ∞, moderately strong confinement would occur. This is the case for TMAAI-containing MCM-41 and SBA-15_1.

The observation of two different guest phases, one amorphous and the other crystalline, emphasizes the need to better classify nanoscale confinement into different possible types. A schematic of these proposed structures is shown in Fig. 4*B*.

Single-molecule confinement occurs when the host dimensions allow only one molecular guest per pore, and due to strong steric effects, the guest molecule is tightly confined without additional space for other molecules. Most zeolites containing SDAs fall into this category (18, 19, 28). In this tight-fit confinement, the guest–host configuration is usually thermodynamically very stable, associated with strong interaction enthalpy (e.g., -176.5 ± 15.0 kJ per mole of TMAAI for SSZ-24). Interacting with the pore walls at several locations, the confined guest has little or no freedom to rotate or diffuse.

As the pore size of the host framework increases, but before crystallization of the guest occurs, a 2D layered or loosely packed cluster-like intermediate guest structure may form in the host. In such a structure, the guest molecules may be adsorbed onto the wall of the framework of the host, either as a monolayer or multilayer, depending on the pore dimension and molecular interactions. Such molecular assemblages are bound with intermediate energies, and the molecules may show temperature-dependent mobility. We call this "multimolecule adsorption/confinement." In the current study, the loosely confined TMAAI in SBA-15_1 (6.6 nm) represents this situation.

If the pore of the host structure is spacious enough to allow the formation of at least a unit cell of the crystal and temperature is below the (depressed) melting point of the guest, crystallization of guest molecules into nanocrystals occurs with spaces separating each crystallite along the axial direction of the cylindrical pores. We call this "nanocrystal confinement." These confined nanocrystals may be structurally distorted and/or disordered, especially near their surfaces, and are presumably higher in free energy than the bulk crystal, but the assemblage of nanocrystals plus host nevertheless represents the minimum free energy accessible under confinement. Due to dimensional restriction from the host structure, further crystal growth is not possible. In this work, SBA-15_2 and 3 are examples of nanocrystal confinement. As noted above, nanocrystals and an amorphous phase can coexist in some cases, e.g., TMAAI confined in mesoporous silicas with pore larger than 12.0 nm.

Although not seen in this work, the nanocrystals under confinement may crystallize in a polymorph other than that seen for the bulk crystal. For example α-glutaric acid, once confined in controlled pore glass, can persist at room temperature for months without detectable phase transformation to its stable bulk phase β-glutaric acid (48). This is a special case of size-induced polymorphism resulting from differences in surface energies or interface energies, discussed in a number of recent papers for unconfined nanocrystals which cannot coarsen at low temperatures (49–52).

Conclusions

Enthalpies of solution for a series of TMAAI-containing porous silica with different pore sizes were measured by HF calorimetry. Coupled with solid-state NMR, TG-DSC, XRD, and IR spectroscopy, the data allowed interaction enthalpies of TMAAI with inorganic porous silica frameworks of different pore size to be calculated, phase occurrence and dynamics of confined guests in pores of various dimensions to be interpreted, and different types of nanoscale inclusion to be described. The states of nanoconfined guest molecules and the strength of guest–host interactions are governed by the pore dimension of the host framework which strongly affects the structure and phase of the confined guest. There appear to be three types of guest inclusion: single-molecule confinement, multimolecule adsorption/confinement, and nanocrystal confinement. The magnitude of interaction enthalpy is a function of the relative size of host pores and guest objects. Understanding the molecular and energetic consequences of these different forms of confinement of organic molecules in nanopores has potential significance for processes as diverse as carbon sequestration, heterogeneous catalysis, and drug delivery.

Materials and Methods

For details, see *SI Materials and Methods*. TMAAI and SSZ-24 were synthesized at Chevron Energy Technology Company, Richmond, California (53). Mesoporous silicas were prepared as previously described (54, 55). The as-made frameworks were calcined at 500 °C. TMAAI-containing porous silicas were prepared by incipient wetness impregnation. Characterization techniques used in this work included powder XRD, infrared spectroscopy (FTIR),

and thermal analysis (TG-DSC). HF solution calorimetry was used to measure the enthalpy of solution as described in our earlier work (21). Solid-state NMR experiments were performed at Caltech. All other experiments were designed and carried out at University of California, Davis.

ACKNOWLEDGMENTS. This work is supported as part of the Center of Nanoscale Control of Geologic CO_2, an Energy Frontier Research Center funded by the US Department of Energy (DOE), Office of Science, Office of Basic Energy Sciences, under Award DE-AC02-05CH11231. The NMR facility at California Institute of Technology (Caltech) was supported by the National Science Foundation (NSF) under Grant 9724240, partially supported by the Materials Research Science and Engineering Centers Program of the NSF under Award DMR-520565, and the US DOE, Office of Energy Efficiency and Renewable Energy, through the Hydrogen, Fuel Cells and Infrastructure Technologies Program under Contract DE-AI-01-05EE11105 (Jet Propulsion Laboratory–Caltech).

1. Mann S, Ozin GA (1996) Synthesis of inorganic materials with complex form. *Nature* 382(6589):313–318.
2. Mann S (1993) Molecular tectonics in biomineralization and biomimetic materials chemistry. *Nature* 365(6446):499–505.
3. Yue WB, Park RJ, Kulak AN, Meldrum FC (2006) Macroporous inorganic solids from a biomineral template. *J Cryst Growth* 294(1):69–77.
4. Yamaguchi A, et al. (2004) Self-assembly of a silica-surfactant nanocomposite in a porous alumina membrane. *Nat Mater* 3(5):337–341.
5. Lai ZP, et al. (2003) Microstructural optimization of a zeolite membrane for organic vapor separation. *Science* 300(5618):456–460.
6. Thomas S, Ali SMF (1989) Flow of emulsions in porous media, and potential for enhanced oil recovery. *J Petrol Sci Eng* 3(1-2):121–136.
7. Sanmiguel JE, Mehta SA, Moore RG (2003) An experimental study of controlled gas-phase combustion in porous media for enhanced recovery of oil and gas. *J Energy ResourTechnol* 125(1):64–71.
8. Farajzadeh R, Andrianov A, Krastev R, Hirasaki GJ, Rossen WR (2012) Foam-oil interaction in porous media: Implications for foam assisted enhanced oil recovery. *Adv Colloid Interface Sci* 183–184:1–13.
9. Mello MR, Phanon D, Silveira GQ, Llewellyn PL, Ronconi CM (2011) Amine-modified MCM-41 mesoporous silica for carbon dioxide capture. *Microporous Mesoporous Mater* 143(1):174–179.
10. Zelenak V, Halamova D, Gaberova L, Bloch E, Llewellyn P (2008) Amine-modified SBA-12 mesoporous silica for carbon dioxide capture: Effect of amine basicity on sorption properties. *Microporous Mesoporous Mater* 116(1-3):358–364.
11. Dutta A, Nandi M, Sasidharan M, Bhaumik A (2012) 3D hexagonal mesoporous silica and its organic functionalization for high CO2 uptake. *ChemPhysChem* 13(13): 3218–3222.
12. Laszlo P (1986) Catalysis of organic-reactions by inorganic solids. *Acc Chem Res* 19(4): 121–127.
13. Takahashi H, et al. (2000) Catalytic activity in organic solvents and stability of immobilized enzymes depend on the pore size and surface characteristics of mesoporous silica. *Chem Mater* 12(11):3301–3305.
14. Taguchi A, Schuth F (2005) Ordered mesoporous materials in catalysis. *Microporous Mesoporous Mater* 77(1):1–45.
15. He QJ, Shi JL (2011) Mesoporous silica nanoparticle based nano drug delivery systems: Synthesis, controlled drug release and delivery, pharmacokinetics and biocompatibility. *J Mater Chem* 21(16):5845–5855.
16. Yang Q, et al. (2005) pH-responsive carrier system based on carboxylic acid modified mesoporous silica and polyelectrolyte for drug delivery. *Chem Mater* 17(24):5999–6003.
17. Vivero-Escoto JL, Slowing II, Wu CW, Lin VSY (2009) Photoinduced intracellular controlled release drug delivery in human cells by gold-capped mesoporous silica nanosphere. *J Am Chem Soc* 131(10):3462–3463.
18. Zones SI, Olmstead MM, Santilli DS (1992) Guest host relationships in the synthesis of large pore zeolite Ssz-26 from a propellane Quaternary ammonium compound. *J Am Chem Soc* 114(11):4195–4201.
19. Zones SI, Nakagawa Y, Yuen LT, Harris TV (1996) Guest/host interactions in high silica zeolite synthesis: [5.2.1.0(2.6)]tricyclodecanes as template molecule. *J Am Chem Soc* 118(32):7558–7567.
20. Nakagawa Y, Lee GS, Harris TV, Yuen LT, Zones SI (1998) Guest/host relationships in zeolite synthesis: Ring-substituted piperidines and the remarkable adamantane mimicry by 1-azonio spiro [5.5] undecanes. *Microporous Mesoporous Mater* 22(1-3): 69–85.
21. Piccione PM, et al. (2000) Thermochemistry of pure-silica zeolites. *J Phys Chem B* 104(43):10001–10011.
22. Trofymluk O, Levchenko AA, Navrotsky A (2012) Mesoporous silica synthesis: Energetics of interaction between framework and structure directing agent. *Microporous Mesoporous Mater* 149(1):119–125.
23. Wu D, Navrotsky A (2013) Small molecule - silica interactions in porous silica structures. *Geochim Cosmochim Acta* 109:38–50.
24. Zhou W, Sun PP, Zhang P, Navrotsky A (2011) Thermochemistry of proton containing borosilicate, aluminosilicate and gallosilicate zeolite beta. *Microporous Mesoporous Mater* 142(2-3):749–753.
25. Zhou W, Navrotsky A, Shin J, Hong SB (2010) Thermochemistry of gallosilicate zeolites with the NAT topology: An energetic view on their in situ disorder-order transformation and thermal stability. *Microporous Mesoporous Mater* 135(1-3):197–200.
26. Sun PP, Deore S, Navrotsky A (2007) Enthalpy of formation and dehydration of lithium and sodium zeolite beta. *Microporous Mesoporous Mater* 98(1-3):29–40.
27. Sun PP, Deore S, Navrotsky A (2006) Formation and dehydration enthalpy of ion exchanged zeolite beta. *Microporous Mesoporous Mater* 91(1-3):15–22.
28. Zones SI (1991) Conversion of faujasites to high-silica chabazite Ssz-13 in the presence of N,N,N-trimethyl-1-adamantammonium iodide. *J Chem Soc Faraday Trans* 87(22): 3709–3716.
29. Brunauer S, Emmett PH, Teller E (1938) Adsorption of gases in multimolecular layers. *J Am Chem Soc* 60(2):309–319.
30. Barrett EP, Joyner LG, Halenda PP (1951) The determination of pore volume and area distributions in porous substances. 1. Computations from nitrogen isotherms. *J Am Chem Soc* 73(1):373–380.
31. Joyner LG, Barrett EP, Skold R (1951) The determination of pore volume and area distributions in porous substances. 2. Comparison between nitrogen isotherm and mercury porosimeter methods. *J Am Chem Soc* 73(7):3155–3158.
32. Patterson AL (1939) The Scherrer formula for X-ray particle size determination. *Phys Rev* 56(10):978–982.
33. Rennie GK, Clifford J (1977) Melting of ice in porous solids. *J Chem Soc Faraday Trans* 1(73):680–689.
34. Rault J, Neffati R, Judeinstein P (2003) Melting of ice in porous glass: Why water and solvents confined in small pores do not crystallize? *Eur Phys J B* 36(4):627–637.
35. Schreiber A, Ketelsen I, Findenegg GH (2001) Melting and freezing of water in ordered mesoporous silica materials. *Phys Chem Chem Phys* 3(7):1185–1195.
36. Jackson CL, Mckenna GB (1990) The melting behavior of organic materials confined in porous solids. *J Chem Phys* 93(12):9002–9011.
37. Alba-Simionesco C, et al. (2003) Confinement of molecular liquids: Consequences on thermodynamic, static and dynamical properties of benzene and toluene. *Eur Phys J E Soft Matter* 12(1):19–28.
38. Jackson CL, McKenna GB (1996) Vitrification and crystallization of organic liquids confined to nanoscale pores. *Chem Mater* 8(8):2128–2137.
39. Tang XP, Ng NC, Nguyen H, Mogilevsky G, Wu Y (2008) The molecular dynamics and melting transition of the confined ibuprofen in titania nanotube studied by NMR. *Chem Phys Lett* 452(4-6):289–295.
40. Hamilton BD, Hillmyer MA, Ward MD (2008) Glycine polymorphism in nanoscale crystallization chambers. *Cryst Growth Des* 8(9):3368–3375.
41. Unruh KM, Huber TE, Huber CA (1993) Melting and freezing behavior of indium metal in porous glasses. *Phys Rev B Condens Matter* 48(12):9021–9027.
42. Azais T, et al. (2006) Solid-state NMR study of ibuprofen confined in MCM-41 material. *Chem Mater* 18(26):6382–6390.
43. Ha JM, Wolf JH, Hillmyer MA, Ward MD (2004) Polymorph selectivity under nanoscopic confinement. *J Am Chem Soc* 126(11):3382–3383.
44. Beiner M, Rengarajan GT, Pankaj S, Enke D, Steinhart M (2007) Manipulating the crystalline state of pharmaceuticals by nanoconfinement. *Nano Lett* 7(5):1381–1385.
45. Rengarajan GT, Enke D, Steinhart M, Beiner M (2008) Stabilization of the amorphous state of pharmaceuticals in nanopores. *J Mater Chem* 18(22):2537–2539.
46. Litvan G, Mcintosh R (1963) Phase transitions of water and xenon adsorbed in porous Vycor glass. *Can J Chem* 41(12):3095–3107.
47. Erko M, et al. (2012) Density minimum of confined water at low temperatures: A combined study by small-angle scattering of X-rays and neutrons. *Phys Chem Chem Phys* 14(11):3852–3858.
48. Ha JM, Hamilton BD, Hillmyer MA, Ward MD (2009) Phase behavior and polymorphism of organic crystals confined within nanoscale chambers. *Cryst Growth Des* 9(11):4766–4777.
49. Ranade MR, et al. (2002) Energetics of nanocrystalline TiO2. *Proc Natl Acad Sci USA* 99 (Suppl 2):6476–6481.
50. Navrotsky A (2004) Energetic clues to pathways to biomineralization: Precursors, clusters, and nanoparticles. *Proc Natl Acad Sci USA* 101(33):12096–12101.
51. Navrotsky A, Mazeina L, Majzlan J (2008) Size-driven structural and thermodynamic complexity in iron oxides. *Science* 319(5870):1635–1638.
52. Navrotsky A, Ma CC, Lilova K, Birkner N (2010) Nanophase transition metal oxides show large thermodynamically driven shifts in oxidation-reduction equilibria. *Science* 330(6001):199–201.
53. Bialek R, Meier WM, Davis M, Annen MJ (1991) The synthesis and structure of Ssz-24, the silica analog of Alpo4-5. *Zeolites* 11(5):438–442.
54. Gallis KW, Landry CC (1997) Synthesis of MCM-48 by a phase transformation process. *Chem Mater* 9(10):2035–2038.
55. Zhao DY, Huo QS, Feng JL, Chmelka BF, Stucky GD (1998) Nonionic triblock and star diblock copolymer and oligomeric surfactant syntheses of highly ordered, hydrothermally stable, mesoporous silica structures. *J Am Chem Soc* 120(24):6024–6036.